Tectonophysics 683 (2016) 77–85

Contents lists available at ScienceDirect

Tectonophysics

journal homepage: www.elsevier.com/locate/tecto

Thrust faulting and 3D ground deformation of the 3 July 2015 Mw 6.4 Pishan, China earthquake from Sentinel-1A radar interferometry

Jianbao Sun [a,*], Zheng-Kang Shen [b], Tao Li [c,a], Jie Chen [a]

[a] State Key Lab. of Earthquake Dynamics, Institute of Geology, China Earthquake Administration, No. 1, Huayanli Jia, Beijing 100029, China
[b] Earth, Planetary, and Space Sciences, University of California, Los Angeles, Los Angeles, CA, USA
[c] Research Institute of Petroleum Exploration and Development, PetroChina, China

ARTICLE INFO

Article history:
Received 3 February 2016
Received in revised form 30 May 2016
Accepted 30 May 2016
Available online 1 June 2016

ABSTRACT

Boosted by the launch of Sentinel-1A radar satellite from the European Space Agency (ESA), we now have the opportunity of fast, full and multiple coverage of the land based deformation field of earthquakes. Here we use the data to investigate a strong earthquake struck Pishan, western China on July 3, 2015. The earthquake fault is blind and no ground break features are found on-site, thus Synthetic Aperture Radar (SAR) data give full play to its technical advantage for the recovery of coseismic deformation field. By using the Sentinel-1A radar data in the Interferometric Wide Swath mode, we obtain 3 tracks of InSAR data over the struck region, and resolve the 3D ground deformation generated by the earthquake. Then the Line-of-Sight (LOS) InSAR data are inverted for the slip-distribution of the seismogenic fault.
The final model shows that the earthquake is completely blind with pure-thrust motion. The maximum slip is ~0.48 m at a depth of ~7 km, consistent with the depth estimate from seismic reflection data. In particular, the inverted model is also compatible with a south-dipping fault ramp among a group of fault interfaces detected by the seismic reflection profile over the region. The seismic moment obtained equals to a Mw 6.4 earthquake. The Pishan earthquake ruptured the frontal part of the thrust ramps under the Slik anticline, and unloaded the coulomb stress of them. However, it may have loaded stress to the back-thrust above the thrust ramps by ~1–4 bar, and promoted it for future failure. Moreover, the stress loading on the west side of the earthquake fault is much larger than that on the east side, indicating a higher risk for failure to the west of the Zepu fault.

1. Tectonic settings of the Pishan earthquake

On July 3, 2015 a Mw 6.4 earthquake struck Pishan, western China. Within a week following the event, 938 M > 1.0 aftershocks were recorded by China Earthquake Data Center (see Data and Resources section). The earthquake caused strong shaking up to magnitude 8 in the epicentral region, and 3 people were killed and 71 were injured due to pervasive collapses of local building structures (http://xj.people.com.cn/n/2015/0706/c362096-25482237.html).

The Pishan earthquake occurred at the southwest rim of the Tarim basin. The northward indentation of the India plate into the Eurasia plate results in wide spread north-south shortening in the Tibetan plateau and the Tian Shan orogen, with the Tarim basin sandwiched in between. South and southwest of Pishan, the West Kunlun and the Karakoram mountains rise up to 6000 m elevation, and along their northern rim multiple strands of thrusts and folds are developed, with the Pishan earthquake inside of the Hetian fold belt. A regional seismic reflection profile (Li et al., 2016; Lu et al., 2016) revealed that in the basin the top 10 km depth is covered with sediments, which is underlain by an early Pleistocene strata containing a series of low-angle detachment ramps. These ramps are part of the frontal fault system which absorbs convergence between the Tibetan plateau and Tarim basin, causing flexure of the basin layer at its southern end. The Pishan earthquake is considered to have ruptured one of such fault ramps, which is identified as the Zepu blind thrust fault (Fig. 1).

About 100 km south of the epicenter lies the Karakash fault striking east–west. This fault connects to the Altyn Tagh fault at its east end, and the latter is a major strike slip fault trending ENE and slipping left-laterally at a rate of ~9 mm/yr to accommodate eastward extrusion of the Tibetau plateau (Bendick et al., 2000; Shen et al., 2001; Zhang et al., 2004). West and southwest of the epicentral region the Karakash fault converges to the Karakoram fault system which strikes northwest and slips right-laterally at a rate of 0–5 mm/yr (Wright et al., 2004a). Crustal deformation rate in the Pishan region is not precisely determined by GPS because of the harsh survey condition in the West Kunlun Mountains region. A study using the campaign dataset from the Crustal Movement Observation Network of China (CMONOC) 1999–2007 showed no obvious motion between stations spanning the southwest

* Corresponding author.
E-mail addresses: sunjianbao@ies.ac.cn (J. Sun), zhengkangshen@gmail.com (Z.-K. Shen), litao.410@163.com (T. Li).

http://dx.doi.org/10.1016/j.tecto.2016.05.051
0040-1951/

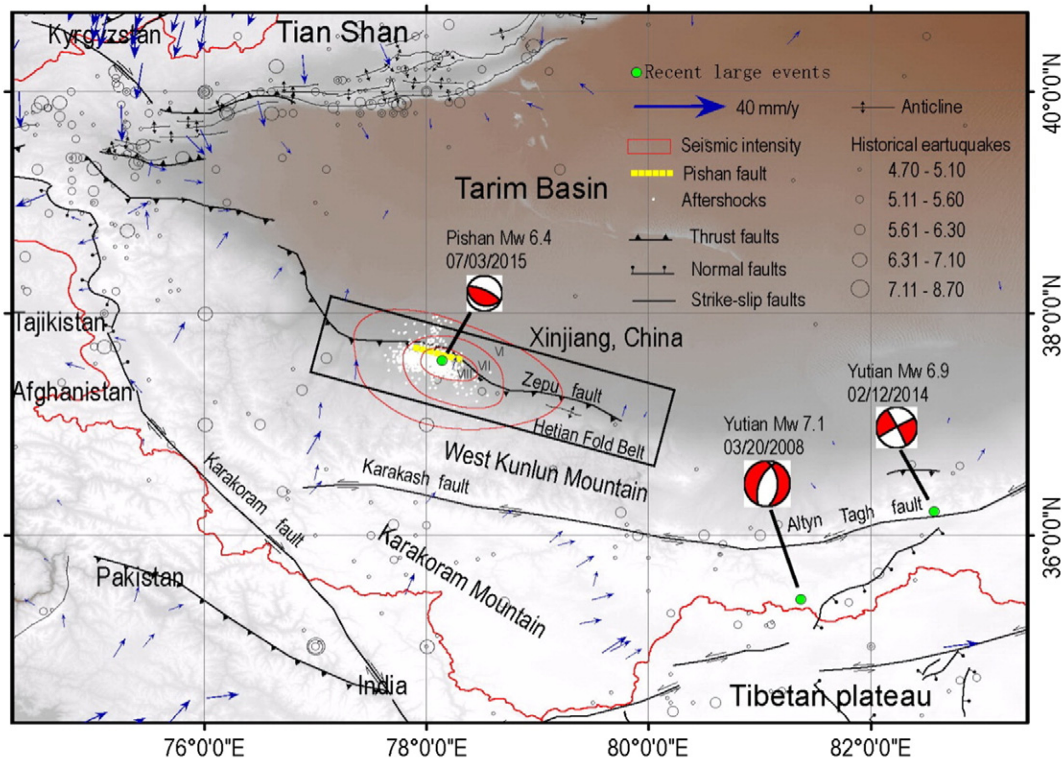

Fig. 1. Tectonic map of western China around the Pishan earthquake region. Fault lines are from Taylor and Yin (2009) and Styron et al. (2010). GPS velocity vectors are updated from Ge et al. (2015), with the sites inside Tarim basin as reference. The background topographic image is the SRTM DEM data (Farr et al., 2007) (see Data and Resources section). The red lines are state borders and administrative boundaries of Chinese provinces. The yellow dashed line is the inferred earthquake fault of this study, projected vertically on the ground. The beach balls show the 2008 Mw 7.1 and 2014 Mw 6.9 Yutian earthquakes, and the Pishan earthquake of this study from the Global Centroid-Moment-Tensor (GCMT) catalog (see Data and Resources section). The white dots indicate the aftershocks during the first week after the earthquake. The red circles show the seismic intensity provided by China Earthquake Administration. The black rectangle shows the Hetian fold belt.

Tarim basin and the West Kunlun Mountains, at the uncertainty of 2 mm/yr (Wang, 2009). A more recent study using the CMONOC datas 2011–2014 yielded a result which also showed no obvious north–south shortening across the region (Ge et al., 2015) (Fig. 1). It however, showed that relative to the sites located in the Tarim basin, the sites located south of the West Kunlun Mountains moved 2–3 mm/yr westward, and the sites located further to the southeast move 3–5 mm/yr southwestward. Such motions might be related to postseismic deformation of the 2008 Mw 7.1 Yutian earthquake whose fault rupture is about 150 km east of these sites. The 2008 Mw 7.1 Yutian earthquake is believed to have significantly altered the Coulomb stress on the Zepu fault. Wan et al. (2010) estimated ~0.16–10.7 bar of Coulomb stress increase on the fault (named as Western Kunlun Mountain Frontal Fault in the paper), with about 5.0 bar Coulomb stress increase at the vicinity of the epicenter of the 2015 Pishan earthquake.

Location of the Pishan earthquake determined by the USGS is at 37.46°N, 78.15°E (see Data and Resources section). The focal depth was estimated as 20.0 km by USGS and 15.6 km by the Global CMT. The focal mechanism solution parameters provided by USGS are: fault strike 98°, dip 34°, and rake 72°. The GCMT solution parameters are: fault strike 109°, dip 22°, and rake 85°. The seismic moment release was estimated as 2.34e + 18 N-m by USGS and 5.33e + 18 N-m by GCMT, corresponding to Mw 6.4 for both cases. Both solutions suggest that the earthquake ruptured a fault which strikes SEE and dips gently SSW, with a dominant thrust component and a minor left-lateral component. Inversion of the rupture process (Zhang Y., personal communication) suggested that the earthquake initiated at the lower part of the fault plane and propagated mostly upward. Aftershocks are concentrated in a region about 50 km wide WNW of the epicenter, suggesting westward propagation of stress release along the fault plane after the quake (Fig. 1).

2. InSAR data and processing

The Sentinel-1A radar satellite of Europe Space Agency (ESA) was launched on 3 April 2014 and the data is available for downloading since May 9, 2014. It acquires C-band synthetic aperture radar (SAR) images using the Interferometric Wide Swath mode (IW) with 12-day revisiting cycles, and will be able to revisit same ground target and form interferometric images with 6-day or less intervals with the Sentiel-1B satellite together (https://sentinel.esa.int/web/sentinel/user-guides/sentinel-1-sar/revisit-and-coverage), compared with the 35-day intervals as their predecessors, ERS-1/2 and Envisat satellites. In addition to help keep high coherence of SAR signals, the short repeat interval is also of particular interests for earthquake studies, due to its capability to capture fast transient deformation following earthquakes. The IW (also called Terrain Observation by Progressive Scans, or TOPS) data has been used for the detection of several large earthquakes, example results can be accessed through insarap.org and http://step.esa.int/main/gallery/, both maintained by ESA. The traditional stripmap mode of Sentinel-1A radar data was also successfully used for InSAR research of the Mw 6.0 Napa Valley earthquake in northern California in 2014 (Elliott et al., 2015). In this study, we try to resolve the 3D ground deformation with IW data, therefore the postseismic data is expected to keep as similar as possible in different tracks to guarantee its reliable estimate. Based on this constraint, we choose the data in Table 1 for deformation detection (see Data and Resources section).

We utilize 3 tracks of SAR data in TOPS mode for InSAR processing, among which one is in descending pass, and the other two are in ascending pass (Table 1). The two ascending pass data capture ground deformation with different sub-swaths in different tracks, so that the incidence angles of the radar waves are as different as ~11.0°. Combining with the descending track data, the imaging geometry of these 3

Table 1
IW/TOPS InSAR data from Sentinel-1A satellite acquired in 2015.

Master date	Slave date	Relative track number[a]	Incidence angle near epicenter (°)	Perpendicular baseline (m)	Delta Doppler Central Frequency (Hz)
June 24	July 18	D136	40.8	27.3	1.1
June 11	July 29	A129	43.8	35.9	3.4
June 11	July 5	A129	43.8	39.5	13.1
June 30	July 24	A056	32.7	−56.3	−2.7

[a] 'D' and 'A' indicate descending and ascending passes of satellite respectively.

tracks makes it possible for 3D deformation calculation. Note that we processed two pairs of SAR data on track 129, with the first post-earthquake data is acquired on July 5, only 2 days after the earthquake. However, in order to keep similar deformation contents in the data and better resolve the 3D deformation, we choose an alternative post-earthquake data acquired on July 29 for further analysis. In addition, the July 5 data has a bit larger Doppler central frequency with the pre-earthquake data of June 11, 2015. This difference is named as Delta Doppler Central Frequency in Table 1, which may lead to slight Doppler central decorrelation of SAR signals (Hanssen, 2001).

We use the open source software, SNAP 2.0 from ESA (see Data and Resources section), to process the data, and assemble 2 or 3 slices of SAR data along tracks for better ground coverage. The precise orbit data from ESA (see Data and Resources section) are applied to improve the InSAR coherence. The SRTM DEM data (Farr et al., 2007) are used for topographic phase removal, and the global optimization algorithm is adopted for phase unwrapping (Strozzi et al., 2008). The Pishan earthquake area is between the south West Kunlun mountains and the north Gobi desert of Tarim basin, where the InSAR data suffer from strong spatial or temporal decorrelation respectively, thus these areas with heavy noise are excluded from processing, while leaving enough data coverage for the earthquake analysis. We also estimate and remove a quadratic ramp from the unwrapping data using the far-field information, then rewrap the interferograms to −π to π radian color cycles for visualization (Fig. 2). The common parts of the 3 interferograms are combined to resolve the 3D ground displacements pixel-by-pixel in a least-square sense.

The 3 tracks of InSAR results show that the major feature of the coseismic deformation is the LOS shortening deformation (negative or blue color in the unwrapping images) close to the Zepu fault, with a much smaller positive feature (red color) connecting with it to the south, no matter the ascending or the descending track is considered. This indicates that the ground deformation is mostly uplift with minor subsidence, which is consistent with a thrust motion underneath the sedimentary and a little subsidence behind the uplift areas in the hanging wall. No more fringes is found in the footwall, this could be the result of a fault ramp motion under the thrust and fold system. The 4 concentrated fringes in the 3 track data are resulted from the uplift motion of the blind thrust faulting, and one fringe of subsidence at most is behind it (Fig. 2a, c and e). Despite of the different atmospheric noise in the data which is particular strong in track A129 data, the InSAR LOS measurements of different incidence angles reflect similar displacement content of the fault motion, hence can be used for 3D displacement decomposition. In contrast to the June 24–July 29 interfergram of track A129, the June 24–July 5 interfergram (see Fig. S1, available in the electronic supplement to this article) shows fewer fringes than the other 3 interferograms used here. This indicates that the early stage afterslip motion is prominent in the first two weeks after the earthquake.

The 3D deformation detection from InSAR phase data is only possible for few cases in previous generation of SAR satellites in near-polar orbit, depending on SAR sensor viewing geometry, such as incidence angles, right-looking or left-looking capabilities etc. A review of the situation can be found in Wright et al. (2004b). A more general case to acquire 3D deformation is to use both phase data and amplitude data, e.g. Fialko et al. (2005). In the new era of SAR technique, epically with the TOPS/IW mode data of Sentinel satellite, fast revisiting with large ground coverage makes it possible for direct 3D measurements using InSAR phase data. The Pishan earthquake of this study is a first case for this purpose. It is straightforward for 3D displacement calculation, given the 3 inputs with 3 different view angles at the common parts of the interferograms. The results show that the east–west component has two opposite motion directions for the east and west part of the imagery, with the eastward motion a bit larger (Fig. 2h). This is a typical feature of a blind thrust fault motion, which was observed by GPS measurements, e.g. the 1994 Northridge earthquake (Shen et al., 1996) and the 2013 Lushan earthquake (Jiang et al., 2014). The north–south component suffers from heavy noise due to the insensitivity of Sentinel-1A data to the motion of this direction (Fig. 2i). This is similar to its predecessors, the ERS and the Envisat satellites. But it is not difficult to qualitatively determine that the motion is northward on the hanging wall of the blind seismic fault, hence the north–south component may help identify the blind source fault. It is also clear that the ground experiences mainly uplift close to the inferred fault slip, and minor subsidence to the south of the uplift area (Fig. 2j). The maximum uplift is ~40.0 rad, or 17.7 cm. Some fringes, e.g. the left half image of Fig. 2c, probably originate partly from the atmospheric delay of InSAR phase, and contribute to the westward motion in Fig. 2h as well.

3. Fault rupture modeling from InSAR deformation data

The ample source of InSAR data and the 3D ground displacements derived from them provide the space-based evidence of seismic fault motion. The double-couple solutions from seismic data (e.g. the GCMT or the USGS solution) help us define the initial model of the blind fault motion, which is also not seen by the on-site field investigations from China Earthquake Administration (Xu C., personal communications). In order to quantitatively invert for the Pishan earthquake fault rupture, we decimate the 3 interferograms in Fig. 2 to discrete points using a quad-tree algorithm (Jonsson et al., 2002)for fault geometry and slip-distribution inversion. For each discrete point, a unique incidence angle corresponding to it is assigned.

Based on a maximizing-a-posteriori probability method (Sun et al., 2013) and the adaptive simulated annealing algorithm (Ingber, 1993), we invert for the blind fault geometry and the slip-distribution of it. The nonlinear parameters are the fault depth and dip. The fault strike is estimated from InSAR interferograms directly, and insensitive to our inversion results (Table 2). The weighting of each data set and the smoothing factor of the slip-solution are determined automatically in the inversion process. We confine the fault to be thrust-dominant, and also allow left-lateral motion by gauging a rake range of 40°–90°, as it is roughly parallel with the Karakash fault to the south.

The inversion results show a fully blind thrust fault located at a depth of ~10 km near the maximum slip (~0.61 m) area, and the fault dips at 32° (model 1 in Table 2, Fig. 3a). The top depth is buried at ~1.95 km depth. The parameters inverted in this study are basically consistent with the results from the inversion of seismic data by various sources; however, the latter show a spread of source parameters when using different data or method (Table 2). Aided by the seismic reflection profile information available for the seismic fault of the Pishan earthquake (Fig. 3), we adopt the fault geometry with its dip as shallow as 16° for the slip inversion, and take it as our preferred final model for

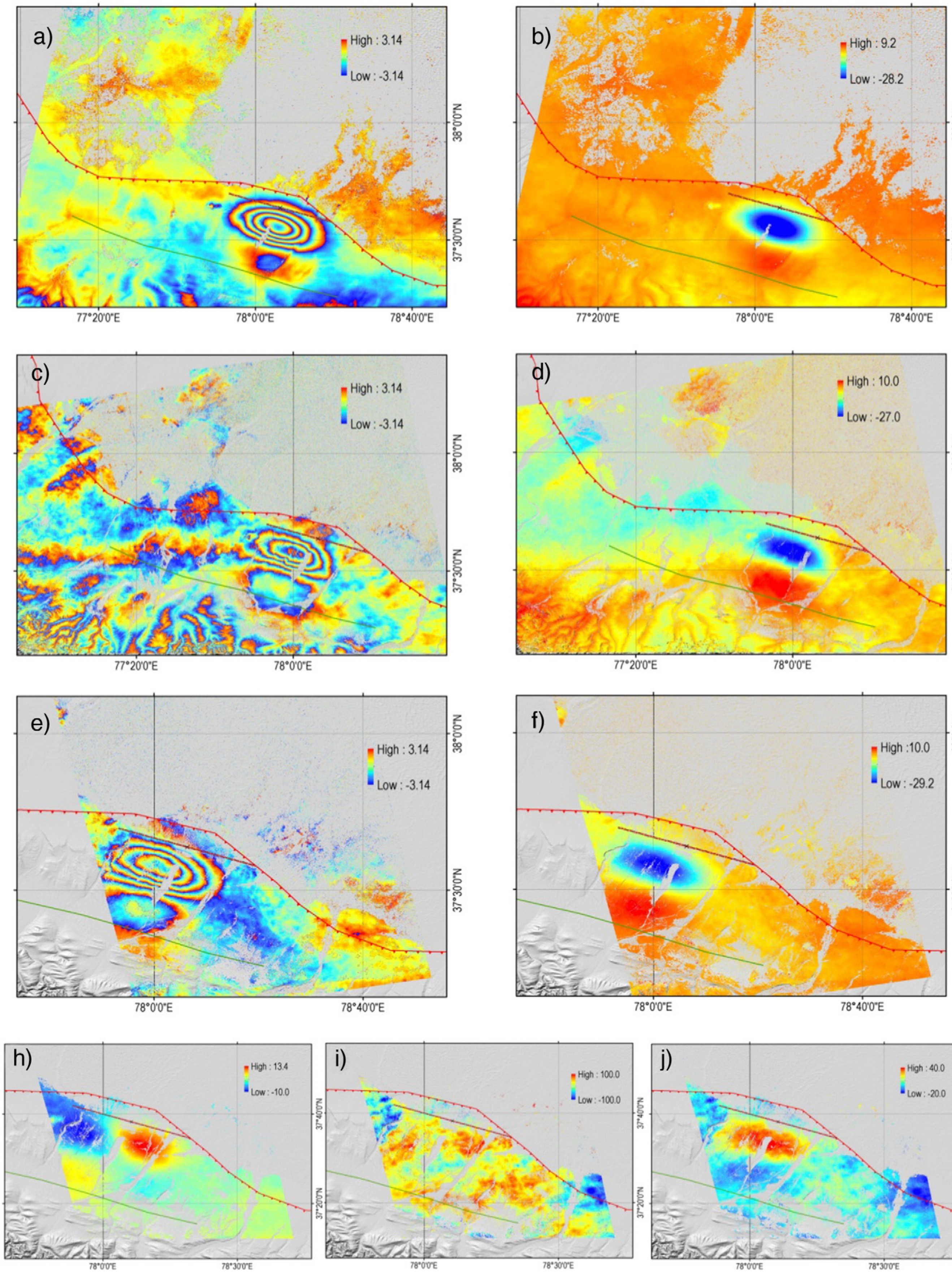
a)
High : 3.14
Low : -3.14
b)
High : 9.2
Low : -28.2
c)
High : 3.14
Low : -3.14
d)
High : 10.0
Low : -27.0
e)
High : 3.14
Low : -3.14
f)
High :10.0
Low : -29.2
h)
High : 13.4
Low : -10.0
i)
High : 100.0
Low : -100.0
j)
High : 40.0
Low : -20.0
77°20'0"E
78°0'0"E
78°40'0"E
78°30'0"E
38°0'0"N
37°30'0"N
37°40'0"N
37°20'0"N

the earthquake (model 2 in Table 2, Fig. 3b), though this model shows a 50% shallower dip than model 1. Justification of model 2 will be discussed in Section 4.2. Note that there is little trade-off effects found between nonlinear parameter pairs in our inversions, and all of the them are reliably determined from the inversion. It however, is difficult to consider the trade-off between the nonlinear parameters and the slip-distribution on the fault plane.

The preferred model gives the shallowest dip than any of the inverted model from seismic or InSAR data only. The seismic moment obtained is similar to that of the seismic models, and equals to a magnitude of Mw 6.4. The maximum slip ~0.48 m with nearly pure thrust motion is detected at a depth of 6.5 km. The significant slip (~0.20 m–0.48 m) occurred at a depth of 4.0–9.0 km, and no meaningful slip can be seen at the upper 4 km, except some strike-slip motion of ~0.02–0.03 m originated maybe from the noise in the data. This is different from the model of He et al. (2016) using Sentinel-1A, ALOS-2 and GPS data, where tens of centimeter slip were obtained and reached the surface, but inconsistent with the field observations from China Earthquake Administration, and the seismic reflection data (Li et al., 2016; Lu et al., 2016). Another group of strike-slip motion of ~0.05–0.1 m occurred at ~8 km–11 km depth (fault bottom). However, the strike-slip displacement is not spatially correlated with the dip-slip motion. The rakes of the significant slip areas are close to 90°, indicating a pure thrust motion of the earthquake fault.

4. Discussion and conclusion

4.1. The residuals of the InSAR inversion models versus the afterslip motion

Both models in Fig. 3 show little displacements at the upper 4 km, however, the slip at the deeper part of them is slightly different. This is probably because the shallow portion of fault slip is well constrained by the InSAR data, while the deeper part of slip suffers from noise in the data, or the mixture of deformation from other mechanisms, such as afterslip, due to the resolution degradation of geodesy observation with depth. In order to analyze the discrepancy between the two models, we present their residuals in Fig. 4 and Fig. S2 for comparison (see Fig. S2, available in the electronic supplement to this article). In model 1 (Table 2), the fault dip is a free parameter, so that the inversion was able to obtain an optimal solution with the highest posteriori probability density function, after testing a range of dips from 10° to 40°. When it is fixed as a constant, or strictly confined in a narrow range of 14°–16°, according to the seismic reflection data, the inversion may not be able to converge to the same solution as the model 1, due to the resolution degradation issues at depth. When the data error is too small to bias the inversion, other fault behavior may prevent the inversion converging to the 'realistic' model. Afterslip following larger earthquakes is a well-known phenomena contributing to surface deformation, hence could influence inversion results besides geodetic data noise. Given the independent constraint from the seismic reflection data for the fault geometry (dip), the inversion can well determine our preferred rupture model, due to the decrease of the degree of freedom. The positive or LOS shortening residuals in 3 tracks of the InSAR data are consistent with a wide and deeper distribution of afterslip motion (Fig. 4). The magnitudes of the residuals are also compatible with the time span of each InSAR data pairs, among which the track D136 data includes the fewest post-seismic deformation, and the track A129 data mixes the most postseismic contribution in the period of data taken, in comparison to the model 1 results (Fig. 3a) and its residuals (see Fig. S2, available in the electronic supplement to this article), in which the inversion found a dipper fault geometry to fit the observations. However, it is hard to discern the variation of the postseismic motion with time from the residuals in Fig. S2 (see Fig. S2, available in the electronic supplement to this article). A clear feature of the LOS lengthening residuals at surface (e.g., see the blue area in Fig. S2c, available in the electronic supplement to this article) indicate that the fault slip in model 1 is overestimated, thus the residuals become negative. This localized residuals may not be unwrapping errors, given the high coherence of the data in track D136. Therefore, we deem that the deeper part afterslip contributes to the InSAR deformation and lead to the inversion residuals in Fig. 4. In order to confirm the existence of the postseismic deformation, we produced an interferogram on track A129 (Fig. S3). It is clear to see that the postseismc deformation between 5 July 2015 and 9 October 2015 are pervasive around the earthquake struck region, and the LOS deformation is as large as one color cycle or ~2.8 cm.

4.2. Justification of model 2 with a priori constraint from the seismic reflection data

Two aspects of evidences support model 2 as our preferred model of the Pishan earthquake. The first one comes from the InSAR data, which have been discussed in Section 4.1. To be more specific, although the inversion residual of model 2 seems larger than that of model 1 (Fig. 4 and Fig. S2, available in the electronic supplement to this article), the weighted residual sum of squares (WRSS) of model 2 is 12.5% less than that of model 1 (2070.7 for model 2 compared to 2367.7 for model 1), when the weight of each data set is considered. In our inversion, the data weights are inverted for as unknowns, with the weights for the data of track A129, D136 and A056 being 3.00, 0.50 and 2.91 respectively for model 2. They are compared with the results of 0.95, 0.82 and 0.73 for the same data sets of model 1. The data weights we obtained can be deemed as the scaling factors of the prior uncertainties (assuming 1.0 cm for each data set), and the posteriori uncertainty is the product of the priori uncertainty and the scaling factor. The weights of model 2 match well with the noise level of the InSAR data in Fig. 2, where at least one additional fringe can be seen on the track A129 data in Fig. 2c, and both track A129 and A056 data cover longer postseismic period and include hence more postseismic deformation. Therefore, we argue that our preferred model 2 can well explain the InSAR observations.

In order to compare the inverse models with the seismic reflection profile, we show the seismic reflection profile and the dip-slip distribution of our preferred model in Fig. 3c and d. The dip-slip displacements of the model 1 is shown in Fig. S4 (see Fig. S4, available in the electronic supplement to this article). The seismic reflection data show a group of fault ramps below the surface between −4 km and −10 km (Fig. 3c). The Slik anticline is directly above these structures. The aftershocks occurred around a short fault ramp between 30 km and 40 km along the north–south direction (Fig. 3c), which corresponds to the Pishan earthquake rupture, and a ~5-km width fault scarp is found above the thrust fault ramp at the surface (Li et al., 2016). A back-thrust above the earthquake rupture merges with it at a wedge tip. The significant slip area of model 2 at 6.0–9.0 km depth corresponds to the fault ramp at the depth of −5.5 to −8.0 km in the seismic reflection profile (note the surface at ~1.0 km here). Above this part of fault, the slip area of the model 2 is shallower than the fault ramp from the seismic reflection profile. This is because the fault ramp becomes flat at its front (fore-thrust) near the wedge tip. To the north of the wedge tip (Fig. 3d), little displacements and few aftershocks occurred. It indicates that the fault motion terminated just at the wedge tip, being consistent

Fig. 2. InSAR deformation field of the Pishan earthquake. (a)–(b), (c)–(d) and (e)–(f) are the rewrapped and unwrapped InSAR phase (in radians) for track D136, A129 and A056 respectively. (h)–(j) are the east, north and up displacement components derived from the 3 unwrapped interferograms in (b), (d) and (f) (in radians). The red and green polylines are the active faults from Taylor and Yin (2009) and Styron et al. (2010). The background image is the SRTM DEM data (Farr et al., 2007). The black-dashed line is the inferred seismic fault projected vertically on the ground.

Table 2
Earthquake source parameters from seismic or InSAR data.

Location	Depth (km)	Dip (°)	Strike (°)	Rake (°)	Seismic moment (N-m)	Data or method	Source
37.58°N 78.14°E	15.6	22	109	85	5.33e + 18	Centroid Moment Tensor[a]	GCMT
37.459°N 78.154°E	23	34	98	72	2.34e + 18	Body wave Moment Tensor	USGS, NEIC
37.459°N 78.154°E	10	22	109	81	4.73e + 18	Centroid Moment Tensor	USGS, NEIC
37.459°N 78.154°E	12.8	34	94	56	4.50e + 18	Centroid Moment Tensor	GCMT, USGS
37.459°N 78.154°E	15.5	24	105	60	5.27e + 18	W-phase Moment Tensor	USGS, NEIC
	6.0–13.0[b]	32	109[c]		4.97e + 18	InSAR	Model 1
	5.0–10.0[b]	16.0[c]	109[c]		4.84e + 18	InSAR	Model 2

[a] Using body waves, intermediate-period surface waves, and mantle waves.
[b] Representing the depth with significant slip occurred on fault plane.
[c] Fixed parameters in the inversion.

with the structure revealed by the seismic reflection profile. Small differences (Fig. 3c and d) could be due to the uniform velocity model assumed in the seismic reflection data inversion (Li et al., 2016). Due to a large dipping angle in model 1, the significant slip area in model 1 (see Fig. S2, available in the electronic supplement to this article) is apparently below the fault ramp by ~2.0 km. Hence, our preferred model is also supported by the seismic reflection data. It is also clear that the aftershocks in the first week distributed mainly above 10-km depth, with few of them occurred below this depth, where no visible slip is inverted for in model 2, but strong slip is found in model 1. In summary, as a fresh case applying the new generation of high-quality TOPS mode SAR data for earthquake deformation detection and inversion, the Pishan earthquake case indicates also that it might still be difficult to uniquely constrain the dipping angle of a blind fault, without assist from other sources, even ample 3D geodetic data available.

4.3. Stress field and seismic hazards of the surrounding regions

We calculate the stress loaded by the Pishan earthquake on its nearby thrust faults inside the Hetian fold belt, with similar fault geometry and motion behavior, and also on a back-thrust fault (Fig. 5), to better define the seismic hazard of the surrounding regions. According to the findings from a geological study (Li et al., 2016), the Slik anticline is not the only structure within the Hetain fold belt, whereas it consists of an array of en echelon folds (Fig. 5). To the south and southwest, the Guman anticline extend ~80 km long and ~14–18 km wide. To the southeast, the Yeheshtagh anticline extend ~50 km long and ~16–22 km wide. The two anticlines are also called the Guman–Yeheshtagh anticline, and share maybe the same thrust system underground (Li et al., 2016). To the northeast, the young and short East Slik anticline is located, but with unknown length. Underneath the Hetian fold belt, the seismic reflection data shows that three near-parallel thrust ramps

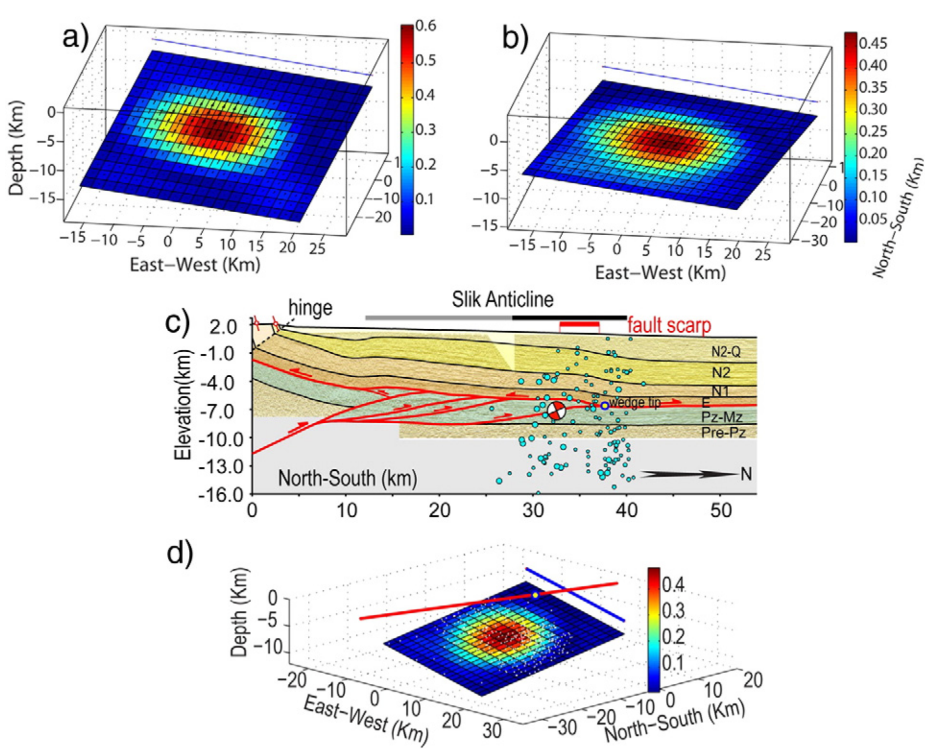

Fig. 3. Slip solutions of the Pishan earthquake. (a) a best-fitting model (Model 1 in Table 2) inverted using LOS InSAR data, with the fault dip and depth as unknowns. The blue line is the surface trace of the seismic fault. (b) similar as model in (a),but with the fault dip fixed at 16° according to the seismic reflection results (Model 2 in Table 2). (c) The seismic reflection cross-section normal to the fault strike at the surface. The filled blue circles show the distribution of the aftershocks. 'N2-Q, N2, N1,E, Pz-Mz and Pre-Pz' represent the strata of Pliocene–Quaternary, Pliocene, Miocene, Paleogene, Paleo-Mesozoic and Pre-Paleozoic respectively. The red lines indicate the fault ramps interpreted according to the seismic reflection data, and the one with a beach-ball on it corresponds to the seismogenic fault of the Pishan earthquake. (d) The dip-slip motion of the seismic fault, with the fault trace (blue) and the seismic reflection profile (red) plotted at the surface. The white dots indicate the aftershock locations during July 3–July 9, 2015. The yellow point inside of a blue circle indicates the wedge tip of the fault ramp underground (c) and at the surface (d). The displacement is in unit of meters.

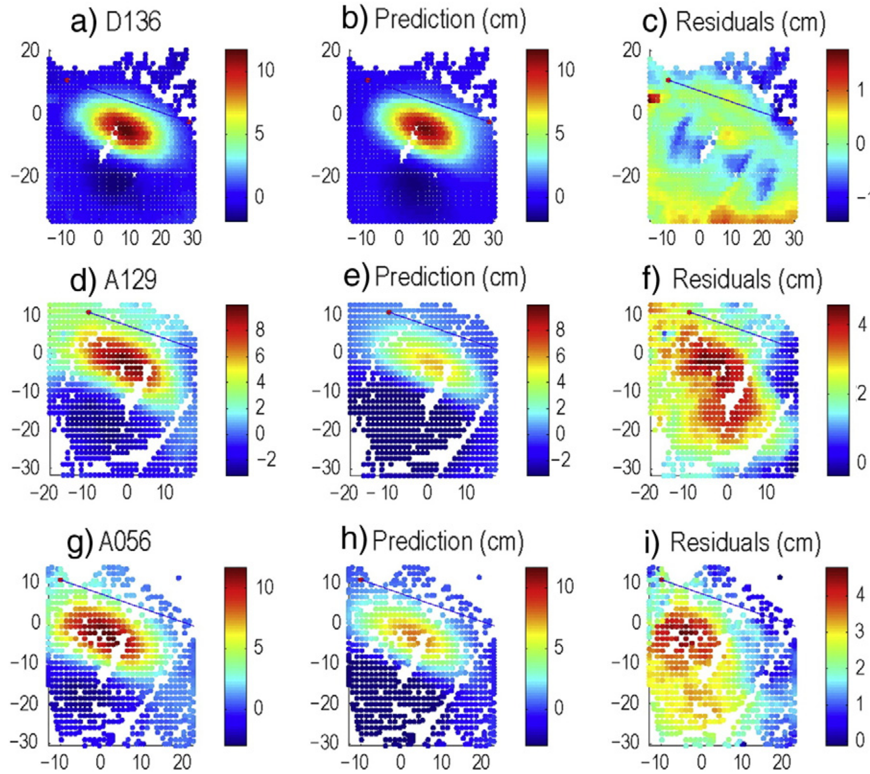

Fig. 4. Model 2 predictions and residuals from InSAR data inversion using a fixed fault dip of 16°. The decimated points, model predictions and residuals of track D136 (a)–(c), track A129 (d)–(f), and track A056 (h)–(j). Unit in centimeters. The blue lines show the vertical projection of the seismic fault on the ground.

soled down to the Hetian South Ramp, and a back-thrust dipping to the north extends from the wedge tip above the Pishan earthquake fault to the south (Fig. 5c). These fault ramps bears the major seismic hazard of the Pishan area and the Hetian fold belt. The Mw 6.4 Pishan earthquake ruptured the front part of the belt, and released part of the seismic energy accumulated in the Hetian fold belt. We calculate the stress changes on the nearby faults by the Pishan earthquake using the Coulomb software from USGS (King et al., 1994) (see Data and Resources section). The results show that the stress loading on the similar south dipping ramps with thrust faulting by the Pishan earthquake are small, and most parts of the faults are out of stress shadow (Fig. 5b). This highlights that the thrust faults behind a ruptured frontal thrust underneath a fold belt are not promoted to failure by the ruptured fault. The upper part of the Pishan earthquake fault with little slip occurred is obviously under the stress shadow, however, the earthquake fault terminates at the wedge tip (Fig. 3c) and the upper part may not able to endure further rupture due to the thick sedimentary above the fault. We do not show the faults under the East Slik anticline and the Yaheshtagh anticline, where they bear little loaded stress from the Pishan earthquake as well. Above the thrust ramp array in Fig. 5b, the flat back-thrust fault extends more than 120 km along strike, with opposite dipping direction to the ramps. The bottom of the back-thrust fault connecting with the Pishan earthquake fault forms a wedge system, and exposes itself under stress shadow. The stress is increased by 1–4 bar on the back-thrust fault near the wedge tip by the Pishan earthquake, and the fault experiences little stress increase to further south (Fig. 5c). Hence the Pishan earthquake promotes the back-thrust fault to future failure, and it could be an potential source of rupture if the future earthquake initiates at the bottom of the back-thrust fault. It is also clear that the coulomb stress at the western end of the Pishan earthquake fault is increase by ~5 bar at 6–7 km depth, however, the eastern end does not show significant stress increase (Fig. 5e). The stress distribution implies that future rupture on the Zepu fault is more likely occurring on the west segment near the Pishan earthquek, rather than on the east nearby segment.

4.4. Conclusions

Take advantage of the new radar satellite, Setinel-1A, from ESA in TOPS/IW mode, we investigate the July 3, 2015 Mw 6.4 Pishan, China earthquake deformation with InSAR technique. Three tracks of radar images were acquired over the seismic region, and cover the earthquake deformation field with 2 ascending and 1 descending passes of SAR data. By combing these data with close postseismic acquisition time, we processed them to extract the full 3D ground deformation. The earthquake deformation in LOS interferograms and 3D components shows that the Pishan earthquake is a blind and pure thrust event with shallowly dipping angle. The new C-band Sentinel-1A data with short revisiting cycles, and wide ground coverage with the TOPS mode, make it possible for quick extraction of 3D ground deformation of earthquakes. The advances of the new radar satellite are superior to its predecessors on earthquake deformation detection, and will definitely promote the SAR data utilization on earthquake science.

By inverse analysis of the Pishan earthquake deformation, we found that the earthquake fault dips 32° to the south, with pure thrust motion. The shallowly dipping fault probably drives the deformation of the fold. By comparing with a seismic reflection profile across the Pishan earthquake area, it is suggested that the earthquake fault is the frontal fault of a series of thrust ramps under the Slik anticline inside the Hetian fold belt. However, the seismic reflection data shows an even shallower dip of 16°. Our analysis indicates that the bias of the dipping angle from its 'realistic' values of 16° may originate from two sources, namely the widely known atmospheric delays of InSAR signals, and/or the early afterslip motion on the deeper part of the fault. The later is well reflected in the InSAR data inversion residuals by assuming a fixed dipping angle of 16°.

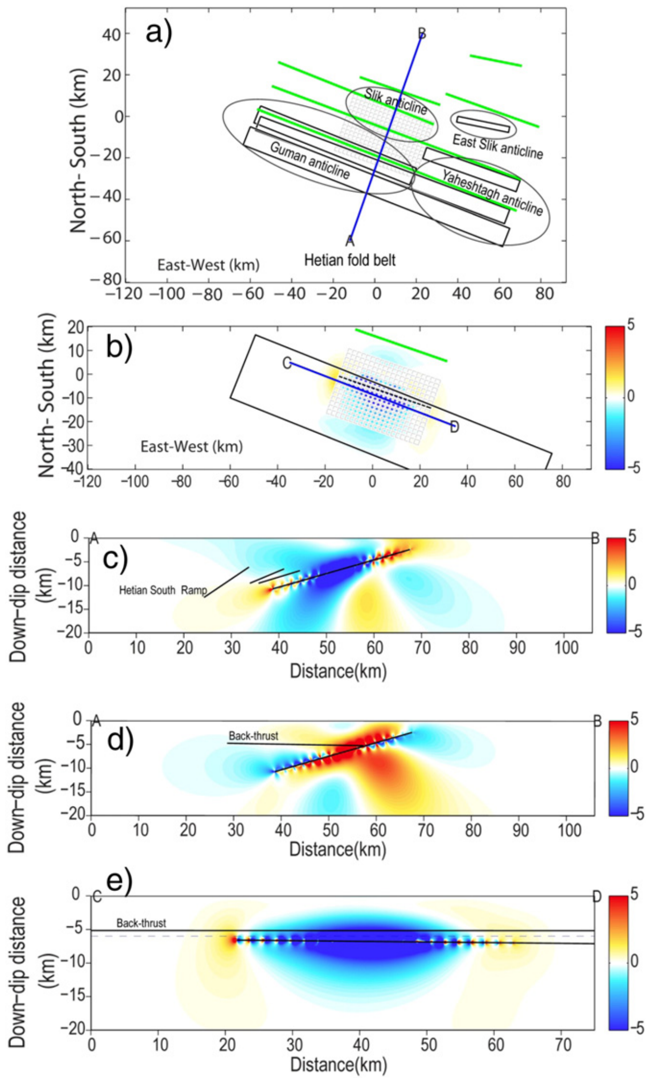

Fig. 5. Static stress changes of the Pishan earthquake. (a) The fault planes of the Pishan earthquake and the nearby thrust faults within the Hetian fold belt projected on the ground. The green lines denote the up-dip projection of the fault traces. The grid shows the Pishan earthquake rupture model, and the rectangles are the fault ramps beneath the nearby anticlines (black circles) from the seismic reflection data (Li et al., 2016). The blue line 'A–B' is the profile across the Pishan earthquake rupture showing in (c) and (d). (b) The coulomb stress changes at 6-km depth on a similar fault to the Pishan earthquake rupture. The rectangle shows the vertical projection of the back-thrust fault on the ground. The blue line 'C–D' is the along strike profile showing in (e). The black line is the 6-km depth of the Pishan earthquake rupture. (c) Coulomb stress changes induced by the Pishan earthquake on the south-dipping ramps with similar geometry and thrust slip. The black lines show the cross-section of the faults. (d) Coulomb stress changes induced by the Pishan earthquake on the north-dipping back-thrust fault with shallow dipping angle. (e) Coulomb stress changes same as in (b), on the 'C–D' profile.

By static stress analysis with the 16° dipping angle model, we found that the Pishan earthquake loaded little stress to the nearby fault ramps, similar to the earthquake fault. However, it promotes the back-thrust fault above the Pishan earthquake fault to failure by 1–4 bar. In addition, it is also clear that the earthquake increases the stress of the western end of the Pishan earthquake rupture more significantly than that of the east end, hence promotes more likely the western segment of the Zepu fault for future rupture in the Hetian fold belt. In a companion study by Li et al. (2016), a large amount of bending-moment fault scarps are found along the Slik anticline crest, which overlaps well with the hanging wall InSAR deformation field of this study. However, no visible ground rupture or break is found in the Pishan earthquake area (Xu C., personal communication). This indicates that the faults in the Hetian fold belt may have the capability to generate more larger earthquakes, although the GPS velocity gradients are ignorable across the faults in the Hetian fold belt.

5. Data and resources

The aftershock data is recorded and made available by China Earthquake Data Center http://data.earthquake.cn/ (last accessed 1 October 2015).

The SRTM DEM data is downloaded from http://srtm.csi.cgiar.org/.

The earthquake focal mechanisms are from the Global Centroid-Moment-Tensor (CMT) catalog http://www.globalcmt.org/CMTsearch.html (last accessed 1 October 2015).

The earthquake location is from USGS http://earthquake.usgs.gov/earthquakes/eventpage/us10002n4w#general_summary (last accessed 1 October 2015).

The Sentinel-1A SAR data is acquired by ESA and available at https://scihub.copernicus.eu/dhus/#/home.

The precise orbit data is from ESA https://qc.sentinel1.eo.esa.int.

The open source software, SNAP 2.0 from ESA, is available at http://step.esa.int/main/.

The Coulomb software is from USGS http://earthquake.usgs.gov/research/software/coulomb/.

Supplementary data to this article can be found online at http://dx.doi.org/10.1016/j.tecto.2016.05.051.

Acknowledgements

The Sentinel-1A radar data is provided by ESA under the Dragon Project No. 10686 of ESA and Ministry of Science and Technology of China. The work is supported by the National Natural Science Foundation of China through project no. 41374040 and no. 41090294. The thoughtful reviews by Qi Wang and an anonymous reviewer are highly appreciated. We also thank Chong Xu of China Earthquake Administration for providing great field investigation photos.

References

Bendick, R., Bilham, R., Freymueller, J., Larson, K., Yin, G.H., 2000. Geodetic evidence for a low slip rate in the Altyn Tagh fault system. Nature 404 (6773), 69–72.

Elliott, J., Hooper, A., Larsen, Y., Marinkovic, P., Wright, T.J., 2015. Earthquake monitoring gets boost from new satellite. EOS Trans. Am. Geophys. Union 96. http://dx.doi.org/10.1029/2015EO023967.

Farr, T.G., et al., 2007. The shuttle radar topography mission. Rev. Geophys. 45 (2), 1–33.

Fialko, Y., Sandwell, D., Simons, M., Rosen, P., 2005. Three-dimensional deformation caused by the bam, Iran, earthquake and the origin of shallow slip deficit. Nature 435 (7040), 295–299.

Ge, W.-P., Molnar, P., Shen, Z.-K., Li, Q., 2015. Present-day crustal thinning in the southern and northern Tibetan plateau revealed by GPS measurements. Geophys. Res. Lett. 42 (13), 5227–5235. http://dx.doi.org/10.1002/2015gl064347.

Hanssen, R.F., 2001. Radar Interferometry: Data Interpretation and Error Analysis (308 pp.) Kluwer Academic Publishers, Dordrecht.

He, P., Wang, Q., Ding, K., Wang, M., Qiao, X., Li, J., Wen, Y., Xu, C., Yang, S., Zou, R., 2016. Source model of the 2015 Mw 6.4 Pishan earthquake constrained by interferometric synthetic aperture radar and GPS: insight into blind rupture in the western Kunlun Shan. Geophys. Res. Lett. 43 (4), 1511–1519. http://dx.doi.org/10.1002/2015gl067140.

Ingber, L., 1993. Simulated annealing: practice versus theory. J Math. Comput. Modell. 18 (11), 29–57.

Jiang, Z., et al., 2014. GPS constrained coseismic source and slip distribution of the 2013 Mw 6.6 Lushan, China, earthquake and its tectonic implications. Geophys. Res. Lett. 41 (2), 407–413. http://dx.doi.org/10.1002/2013gl058812.

Jonsson, S., Zebker, H., Segall, P., Amelung, F., 2002. Fault slip distribution of the 1999 mw 7.1 Hector Mine, California, earthquake, estimated from satellite radar and GPS measurements. Bull. Seismol. Soc. Am. 92 (4), 1377–1389.

King, G.C.P., Stein, R.S., Lin, J., 1994. Static stress changes and the triggering of earthquakes. Bull. Seismol. Soc. Am. 84 (3), 935–953.

Li, T., Chen, J., Fang, L., Zhuxin, C., Jessica, T.A., Jia, C., 2016. The 2015 Mw 6.4 Pishan earthquake: seismic hazards of an active blind wedge thrust system at the Western Kunlun range front, northwest Tibetan plateau. Seismol. Res. Lett. 87 (3), 601–608.

Lu, R., Xu, X., He, D., Liu, B., Tan, X., Wang, X., 2016. Coseismic and blind fault of the 2015 Pishan Mw 6.5 earthquake: implications for the sedimentary-tectonic framework of the western Kunlun Mountains, northern Tibetan Plateau. Tectonics http://dx.doi.org/10.1002/2015tc004053 (n/a-n/a).

Shen, Z.-K., Ge, B.X., Jackson, D.D., Potter, D., Cline, M., Sung, L.-y., 1996. Northridge earthquake rupture models based on the global positioning system measurements. Bull. Seismol. Soc. Am. 86 (1B), S37–S48.

Shen, Z.-K., Wang, M., Li, Y., Jackson, D.D., Yin, A., Dong, D., Fang, P., 2001. Crustal deformation along the Altyn Tagh fault system, western China, from GPS. J. Geophys. Res. 106 (B12), 30,607–630,621.

Strozzi, T., Kouraev, A., Wiesmann, A., Wegmüller, U., Sharov, A., Werner, C., 2008. Estimation of Arctic glacier motion with satellite L-band SAR data. Remote Sens. Environ. 112 (3), 636–645. http://dx.doi.org/10.1016/j.rse.2007.06.007.

Styron, R., Taylor, M., Okoronkwo, K., 2010. Database of active structures from the Indo-Asian collision, *Eos*. Trans. Am. Geophys. Union 91 (20), 181–182. http://dx.doi.org/10.1029/2010eo200001.

Sun, J., Shen, Z.-K., Bürgmann, R., Wang, M., Chen, L., Xu, X., 2013. A three-step maximum-A-posteriori probability method for InSAR data inversion of coseismic rupture with application to the April 14, 2010 Mw 6.9 Yushu, China earthquake. J. Geophys. Res. Solid Earth http://dx.doi.org/10.1002/jgrb.50244 (n/a-n/a).

Taylor, M., Yin, A., 2009. Active structures of the Himalayan–Tibetan orogen and their relationships to earthquake distribution, contemporary strain field, and Cenozoic volcanism. Geosphere 5 (3), 199–214. http://dx.doi.org/10.1130/ges00217.1.

Wan, Y., Shen, Z.-K., Sheng, S., 2010. The mechanical effects of the 2008 Ms7.3 Yutian, Xinjing earthquake on the neighboring faults and its tectonic origin of normal faulting mechanism. Chin. J. Geophys. (Chin.) 53 (2), 280–289. http://dx.doi.org/10.3969/j.issn.0001-5733.2010.02.006.

Wang, M., 2009. Analysis of GPS Data with High Precision and Study on Present-Day Crustal Deformation in China (PhD. thesis, 95 pp.) Inst. Geology, China Earthq. Admin.

Wright, T., Parsons, B., England, P.C., Fielding, E.J., 2004a. InSAR observations of low slip rates on the major faults of western Tibet. Science 305 (5681), 236–239.

Wright, T., Parsons, B., Lu, Z., 2004b. Toward mapping surface deformation in three dimensions using InSAR. Geophys. Res. Lett. 31. http://dx.doi.org/10.1029/2003GL018827.

Zhang, P.Z., Shen, Z., Wang, M., Gan, W.J., Burgmann, R., Molnar, P., 2004. Continuous deformation of the Tibetan plateau from global positioning system data. Geology 32 (9), 809–812.